

Article

Electrochemical Impedance Spectroscopy-Based Characterization and Modeling of Lithium-Ion Batteries Based on Frequency Selection

Yuechan Xiao ^{1,†}, Xinrong Huang ^{1,†}, Jinhao Meng ², Yipu Zhang ^{1,*}, Vaclav Knap ³ and Daniel-Ioan Stroe ^{4,*}

¹ School of Energy and Electrical Engineering, Chang'an University, Xi'an 710018, China; xiaoyuechan@chd.edu.cn (Y.X.); hxr@chd.edu.cn (X.H.)

² School of Electrical Engineering, Xi'an Jiaotong University, Xi'an 710049, China; jinhao@xjtu.edu.cn

³ Department of Electrotechnology, Czech Technical University in Prague, 16627 Prague, Czech Republic; vaclav.knap@cvut.cz

⁴ Department of Energy, Aalborg University, 9220 Aalborg, Denmark

* Correspondence: zyipu@chd.edu.cn (Y.Z.); dis@energy.aau.dk (D.-I.S.)

† These authors contributed equally to this work.

Abstract: Lithium-ion batteries are commonly employed in electric vehicles due to their efficient energy storage and conversion capabilities. Nevertheless, to ensure reliable and cost-effective operation, their internal states must be continuously monitored. Electrochemical impedance spectroscopy (EIS) is an effective tool for assessing the battery's state. Different frequency ranges of EIS correspond to various electrochemical reaction processes. In this study, EIS measurements were conducted at seven temperatures, ranging from -20°C to 10°C , and across 21 states of charge (SOCs), spanning from 0% to 100%. A regression model was utilized to examine the unidirectional factorial characteristic impedance relative to temperature and SOC. An analysis of variance (ANOVA) table was created with temperature and SOC as independent variables and the impedance value as the dependent variable. These models accurately capture the behavior of lithium-ion batteries under different conditions. Based on this research, the battery electrochemical processes are better understood. This paper establishes a mathematical expression for a temperature–SOC-based impedance model at specific frequencies, i.e., 1 Hz, 20 Hz, and 3100 Hz. When comparing the models at these three frequencies, it was found that the model fitting accuracy is highest at 20 Hz, making it applicable across a wide range of temperatures and SOCs. Consequently, the accuracy of the impedance model can be enhanced at a specific frequency, simplifying the impedance model and facilitating the development of advanced battery state estimation methods.



Academic Editor: King Jet Tseng

Received: 17 November 2024

Revised: 20 December 2024

Accepted: 23 December 2024

Published: 29 December 2024

Citation: Xiao, Y.; Huang, X.; Meng, J.; Zhang, Y.; Knap, V.; Stroe, D.-I.

Electrochemical Impedance

Spectroscopy-Based Characterization and Modeling of Lithium-Ion Batteries Based on Frequency Selection. *Batteries* **2025**, *11*, 11. <https://doi.org/10.3390/batteries11010011>

Copyright: © 2024 by the authors. Licensee MDPI, Basel, Switzerland. This article is an open access article distributed under the terms and conditions of the Creative Commons Attribution (CC BY) license (<https://creativecommons.org/licenses/by/4.0/>).

Keywords: lithium-ion battery; electrochemical impedance spectroscopy; temperature; state of charge; modeling

1. Introduction

Electric vehicles (EVs) have experienced rapid development recently; global EV sales reached 14,653,000 units in 2023, a growth of 35.4% since 2022 [1]. Lithium-ion batteries have become the dominant energy storage technology for electric vehicles (EVs) due to their high energy density and high efficiency [2–4].

Realistic monitoring of the battery states is significant. The degradation and improper operation of lithium-ion batteries seriously affect their performance. Therefore, Li-ion batteries require the battery management system (BMS) to ensure safe and efficient operation during their lifetime. This is usually achieved directly by obtaining information, such as battery current,

voltage, and temperature, to estimate the battery's states. However, this information cannot characterize the internal mechanism of the battery. Electrochemical impedance spectroscopy (EIS) can be used to analyze the electrode process kinetics, bilayer, and diffusion of a battery to obtain impedance information over a wide frequency range. Compared with the traditional method of relying on the current, voltage, and temperature [5] to determine the battery state, EIS-based methods allow for more dynamic information and structural information of the electrode interface [6,7]. It has the advantage of non-destructive and *in situ* measurements [7], compared with the physical and chemical characterization techniques, such as X-ray photo-electron spectroscopy [8], scanning electron microscopy [9,10], and Raman spectroscopy [11]. Lithium-ion batteries are modeled by electrochemical models and equivalent circuit models (ECMs) [12,13]. Electrochemical models are relatively accurate in their predictions, but are more complex. For example, the pseudo-two-dimensional model (P2D) is based on porous electrode theory, concentrated solution theory, and kinetic equations [14] and has been widely used in lithium-ion battery research [15]. The second-order RC circuit model based on the hybrid pulse power characterization (HPPC) test [16], which focuses on transient power and internal resistance and does not provide frequency response information, limits the in-depth understanding of the complex electrochemical processes inside the battery. The development of BMS needs to overcome the complexity of battery modeling and improve the accuracy of state estimation. EIS, as a powerful tool, is essential for understanding and simulating battery behavior, developing dynamic models, and improving the performance of BMS. While invasive techniques can provide a more in-depth understanding of battery degradation mechanisms, non-invasive techniques such as EIS are preferred for practical BMS applications due to their reliability and cost-effectiveness. The use of EIS in conjunction with ECM provides an effective means of real-time monitoring and control of the battery state, which helps to improve BMS performance and battery lifetime [17,18]. EIS testing generally involves applying a series of small-amplitude AC potential waves of varying frequencies to the battery. The battery impedance is solved for based on the ratio of voltage to current. Finally, the impedance and the impedance phase angle of the battery at different frequencies can be contained. A Nyquist diagram can be plotted to describe the impedance characteristics of the battery.

Impedance has been widely used as a metric for developing battery models [19,20]. Many studies have utilized different equivalent frequencies, circuit elements, and portions of impedance for state of charge (SOC) estimation [21–23], state of health (SOH) estimation [24,25], and internal temperature (IT) estimation [26–28]. Refs. [7,21,29] proposed a new EIS-based model-updating strategy for SOC algorithms to correct the model parameters based on the rate of change in ohmic impedance during the aging process. The model-corrected SOC estimation error can be controlled within 5.4%. Ref. [7] identifies and quantifies the correlation between each impedance variable and frequency. The potential of impedance spectra based on specific frequencies for estimating battery SOC was verified. Ref. [29] identified the maximum peak frequency and phase angle as suitable parameters for predicting the SOC of Li-ion batteries. Thus, they are used for SOC prediction. The key frequency characteristics for SOC estimation were extracted by the authors of [23], and this SOC estimation method, which takes into account the ambient temperature and lithium-ion diffusion process, outperforms the traditional methods in terms of accuracy and computational efficiency. In [24], a probabilistic model of charge transfer resistance, temperature, and SOC was used to estimate SOH. The estimation error of this method is about 4%. Ref. [25] shows that excellent performance can be obtained in battery SOH estimation by utilizing fixed-frequency impedance features. In [26], internal temperature estimation is realized by obtaining the phase shift and magnitude of the impedance at a selected excitation frequency. The effectiveness of the method is experimentally verified, and how the method can be integrated into a BMS for engineering applications is shown.

In [27], the IT is estimated by selecting the excitation frequency. This method yields more accurate temperature estimates with a root mean square (RMS) deviation of $0.4\text{ }^{\circ}\text{C}$ and a mean standard deviation of $0.7\text{ }^{\circ}\text{C}$. The temperature estimation model in the literature [28] is based on a characteristic frequency point of 200 Hz and has been shown through multiple cell and cycle validations to be an accurate and reliable temperature prediction tool with an average root mean square error of $1.41\text{ }^{\circ}\text{C}$ in the estimated temperature. The imaginary part, real part, and phase of the impedance at different frequencies were used in various studies, such as 10 kHz [30], 630 Hz [31], 300 Hz [32], 215 Hz [33], and 40 Hz [34] for IT estimation. The model's accuracy varies with frequency. Therefore, investigating the accuracy across different frequencies is crucial for improving battery state estimation.

This work studies the effect of impedance frequency on model accuracy by considering a wide SOC and temperature range. The battery impedance is determined by considering various SOCs and temperatures to obtain more accurate correlation coefficients. The strength of this correlation was then quantified using regression equations and ANOVA tables. Finally, the temperature–SOC-total impedance is modeled considering different frequencies, i.e., 1 Hz, 20 Hz, and 3100 Hz. The results show that the impedance model at 20 Hz not only has high model accuracy but also applies to a wide range of conditions. Unlike existing studies, this paper includes a quantification of the extent to which temperature and SOC affect impedance. In addition, this paper compares the temperature–SOC-impedance models at different frequencies and obtains a frequency with a high model accuracy and a wide range of applicability.

The paper is structured as follows. Section 2 analyzes the electrochemical behavior of the battery at different frequencies through Nyquist curves and establishes an equivalent circuit model. Section 3 shows the experimental design flow, and analyzes the trend of the battery impedance characteristics with temperature and SOC based on the test results. In Section 4, a regression analysis of the one-way factorial characteristic impedance of temperature and SOC is performed. It is investigated how temperature and SOC individually affect the impedance characteristics of lithium-ion batteries. An ANOVA table is created to numerically reflect the degree of influence of ambient temperature and SOC on battery impedance. The temperature–SOC-total impedance model is established by selecting specific frequencies at different frequency ranges. Section 5 gives the conclusions of this paper.

2. Impedance Model

The combination of EIS and ECM is a powerful method used to deeply characterize and understand the properties of lithium-ion batteries. The dynamic behavior of the cell is described more comprehensively by fitting different frequency bands to the EIS curve [18]. Figure 1 shows an example of EIS divided into four frequency ranges [35]:

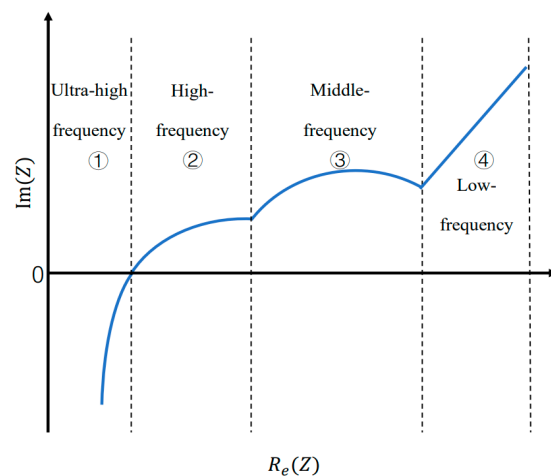


Figure 1. Nyquist impedance spectrum of the lithium-ion battery.

(1) Ultra-high frequency range arc (①): it is the inductive behavior of electrons through wires and internal electrode entanglements, etc., and can be expressed in terms of the equivalent element L . In addition, the portion of the curve intersecting the real axis represents the ohmic internal resistance of the battery, which can be expressed by the element R_0 [36].

The total impedance of the composite element consisting of R_0 and L is expressed as follows:

$$Z = R_0 + j\omega L \quad (1)$$

(2) High-frequency band semicircle (②): it is generated by the diffusion of Li⁺ through the Solid Electrolyte Interface Film (SEI) on the surface of the electrode active material, which is represented by R_{SEI} and CPE_{SEI} in parallel. R_{SEI} represents the internal resistance of the SEI formed at the electrode interface. The constant phase angle component CPE_{SEI} represents the capacitance effect of the SEI [12].

The complex impedance $Z_{CPE_{SEI}}$ of CPE_{SEI} is described as follows:

$$Z_{CPE_{SEI}} = \frac{1}{(j\omega)^{n_{SEI}} Q_{SEI}} \quad (2)$$

where ω is the frequency and j is the imaginary part of the impedance. CPE_{SEI} is the coefficient of the constant phase element Q_{SEI} and n_{SEI} is the attenuation factor. $Z_{R_{SEI}}$ is given by the following equation:

$$Z_{R_{SEI}} = \frac{1}{1/R_{SEI} + (j\omega)^{n_{SEI}} Q_{SEI}} \quad (3)$$

(3) Middle-frequency semicircle (③): it is expressed in parallel with R_{ct} and CPE_{ct} . R_{ct} represents the internal resistance of the electrode to charge transfer; CPE_{ct} denotes the response characteristics after the generation of dispersion effects [37].

The complex impedance $Z_{CPE_{ct}}$ of CPE_{ct} is described as follows:

$$Z_{CPE_{ct}} = \frac{1}{(j\omega)^{n_{ct}} Q_{ct}} \quad (4)$$

where Q_{ct} and n_{ct} are the same as defined in $Z_{CPE_{ct}}$. The complex impedance $Z_{R_{ct}}$ of the combined element is given as follows:

$$Z_{R_{ct}} = \frac{1}{1/R_{ct} + (j\omega)^{n_{ct}} Q_{ct}} \quad (5)$$

(4) Low-frequency band slash (④): it is generated by Li⁺ diffusion processes near the electrode interface and in the active material, which can be expressed by describing the Warburg impedance W [38]. To simplify the model, the low-frequency band is not considered.

Figure 2 shows the simplified ECM based on EIS; the battery impedance can be expressed as follows:

$$Z_{ECM} = R_0 + j\omega L + \frac{1}{1/R_{SEI} + (j\omega)^{n_{SEI}} Q_{SEI}} + \frac{1}{1/R_{ct} + (j\omega)^{n_{ct}} Q_{ct}} \quad (6)$$

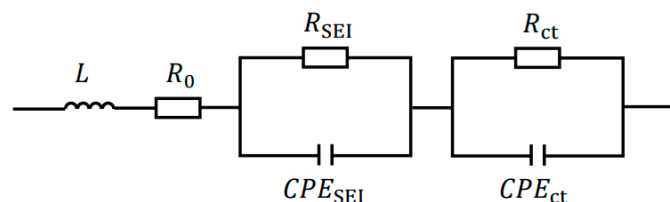


Figure 2. Second-order ECM.

3. Experiment Method

The experiment is performed using a NCR18650GA power lithium-ion battery manufactured by Panasonic in Shenzhen, China. The battery parameters are given in Table 1. The temperature chamber is MHW-200 produced by NEWARE in Shenzhen, China, which enables the tested battery to stay in a specific constant-temperature environment. The electrochemical workstation is MULTI AUTOLAB M204, produced by Metrohm in Beijing, China, measuring the battery EIS. The experimental platform is presented in Figure 3.

Table 1. Battery parameters.

Model	18650
Nominal capacity	3500 mAh
Nominal voltage	3.7 V
Anode material	Li(NiCoMn)O ₂
Cathode material	Plumbago
Battery internal resistance	25 mΩ
Charge cut-off voltage	4.2 V
Discharge cut-off voltage	2.5 V
Charge cut-off current	0.02 C
Format	Cylindrical, 18650
Weights	48 g
Operating temperature range	Charge: 10–45 °C Discharge: –20–60 °C

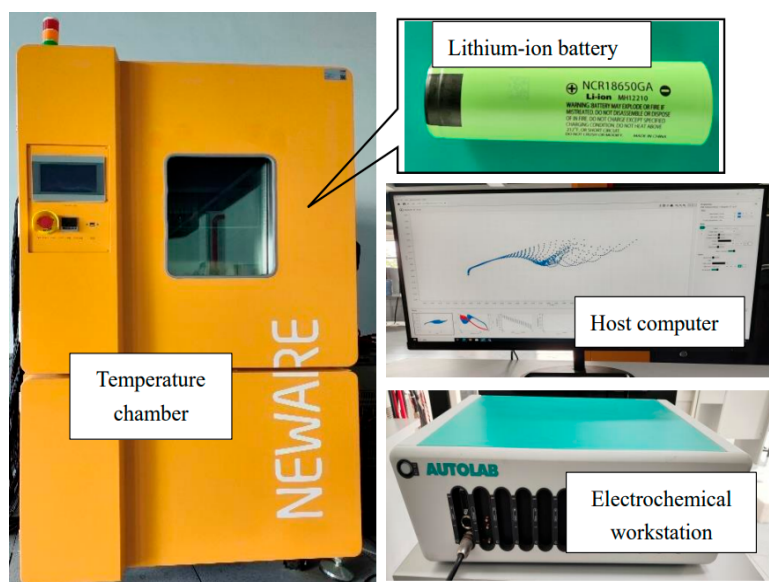


Figure 3. Experimental platform used for EIS parametrization of selected Li-ion battery cell.

3.1. Experimental Procedure

(1) Pre-testing: Leave the battery at 20 °C for 2 h. Fully charge the battery cell using the constant current–constant voltage (CC-CV) mode, and the current of the CC phase and cut-off charging current of the CV phase are 0.2 C (0.7 A) and 0.02 C (0.07 A), respectively; discharge the battery with 0.2 C until the discharging cut-off voltage. Repeat these processes three times.

(2) Capacity test: Leave the battery at 20 °C for 2 h. Fully charge the battery cell using the CC-CV mode, and the constant current of the CC phase and cut-off charging current of the CV phase are 0.2 C (0.7 A) and 0.02 C (0.07 A), respectively; discharge the battery with 0.2 C until the discharging cut-off voltage. The discharging capacity is regarded as the battery nominal capacity at 20 °C.

- (3) Place the battery at 20 °C for 2 h.
- (4) Fully charge the battery unit using the CC-CV mode.
- (5) Place the battery at 20 °C for 2 h.
- (6) Measure the EIS of the battery considering an AC signal amplitude of 5 mV and a frequency range set from 0.001 Hz to 10,000 Hz.
- (7) Place the battery at 20 °C for 2 h.
- (8) Discharge the battery with 0.2 C for 5% SOC.
- (9) Place the battery at 20 °C for 15 min.
- (10) Repeat steps (6)–(9) for all SOCs, with 5% SOC increments.
- (11) Repeat steps (2)–(10) at the following temperatures: –20 °C, –15 °C, –10 °C, –5 °C, 0 °C, 10 °C, and 20 °C.

3.2. Experimental Results

The impedance spectrum-fitting software ZView2 is used to fit the EIS to determine the model parameters, as shown in Figure 4. The fitting errors are shown in Table 2.

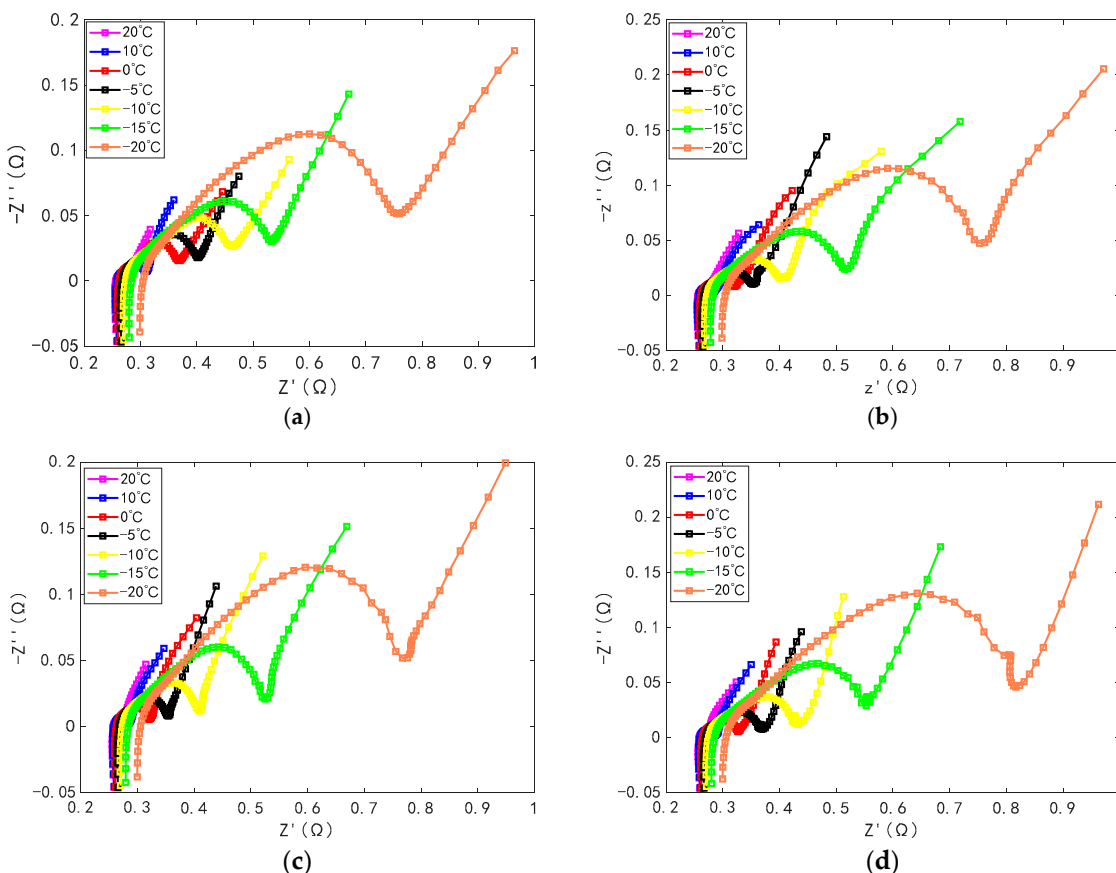


Figure 4. Dependency of the impedance spectra on temperature at different SOCs: (a) SOC = 100%; (b) SOC = 80%; (c) SOC = 60%; (d) SOC = 40%.

Table 2. Fitting errors for each equivalent element.

Parameters	L	R_0	R_{SEI}	Q_{SEI}	n_{SEI}	R_{ct}	Q_{ct}	n_{ct}
Error (%)	0.26 ± 0.08	0.11 ± 0.05	0.73 ± 0.07	1.82 ± 0.3	0.63 ± 0.07	0.13 ± 0.06	3.34 ± 0.5	0.97 ± 0.1

Figure 4 shows the battery impedance under different conditions. In the ultra-high frequency band, the intersection of the curve with the real axis gradually shifts to the right as the temperature decreases; i.e., the battery R_0 increases with decreasing temperature. Therefore, the ohmic resistance has a negative correlation with the temperature, as shown

in Figure 5a. The main reason is that the ohmic internal resistance of lithium-ion batteries mainly originates from the positive and negative electrode materials, electrolyte, and separator, where the electrolyte has a significant contribution. However, the electrolyte is sensitive to temperature, especially at low temperatures, which can lead to an increase in the viscosity of the electrolyte and a decrease in the conductivity of the ions in the electrolyte, thus increasing the ohmic resistance. In the high-frequency and mid-frequency bands, the depressed semicircles characterizing R_{SEI} and R_{ct} increase as the temperature decreases; nevertheless, the increase is more significant for the charge transfer resistance. Both R_{SEI} and R_{ct} increase exponentially and are significantly affected by the low temperature, as shown in Figures 6a and 7a. The main reason for this is that both the Li⁺ volume concentration and diffusion coefficient decrease with decreasing temperature, and the resistance to Li⁺ transport through the SEI layer increases. The low temperature decreases the chemical reaction rate and the efficiency of the ions' transport, and thus increases the resistance at the electrolyte–electrode interface.

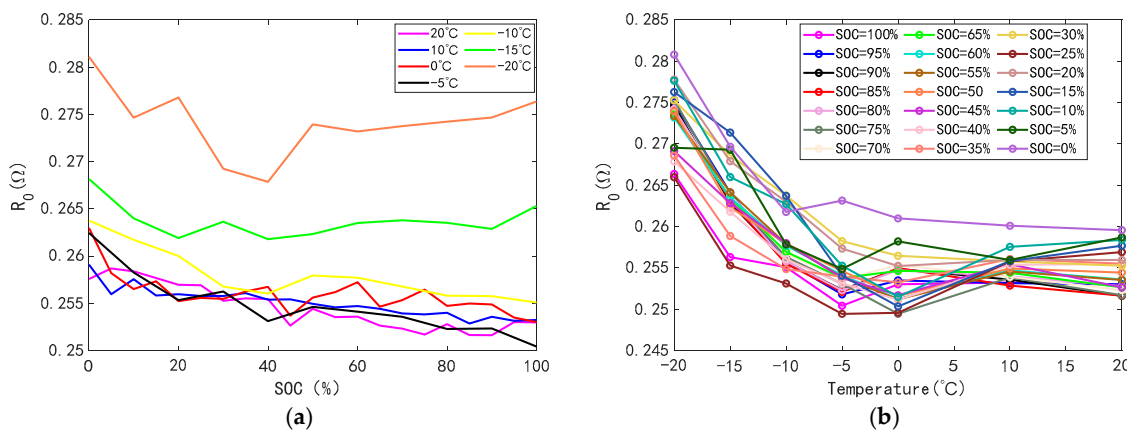


Figure 5. Dependence on measurement conditions of ohmic resistance R_0 : (a) R_0 versus SOC curve; (b) R_0 versus temperature curve.

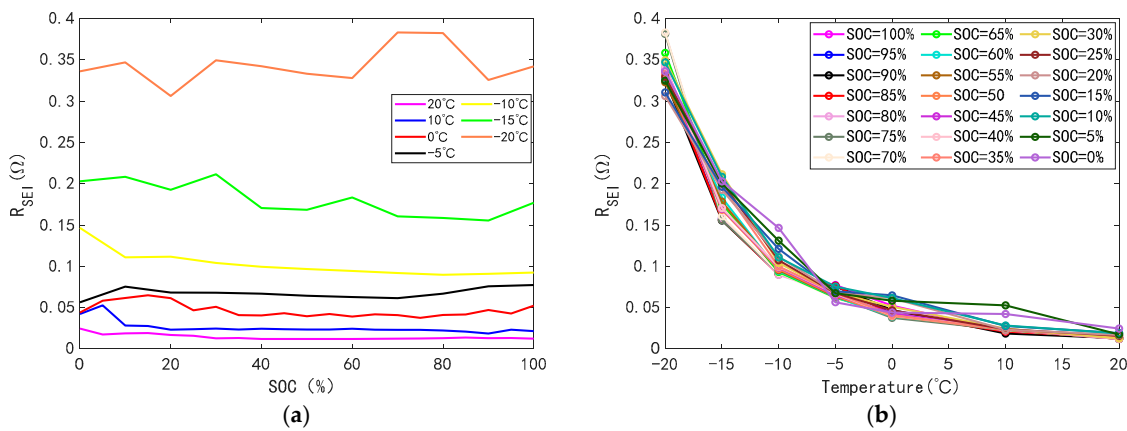


Figure 6. Dependence on measurement conditions of SEI resistance R_{SEI} : (a) R_{SEI} versus SOC curve; (b) R_{SEI} versus temperature curve.

In Figure 5, R_0 increases with the decrease in the SOC, but the magnitude of the increase is not significant. R_0 is mainly composed of the resistance of the electrolyte, electrode materials, and collectors inside the cell. However, the SOC usually does not directly affect the ohmic resistance as it mainly depends on the intrinsic resistivity of the material and the geometry of the cell. In Figure 8, the diameters of the two depressed semicircles gradually increase with the decrease in SOC in the high- and middle-frequency bands. This is due to the reaction conditions at the electrode surface not being favorable

for rapid charge transfer under low-SOC conditions. This leads to an increase in R_{SEI} , and R_{ct} . The effect of SOC on R_0 , R_{SEI} , and R_{ct} is not significant compared to temperature. This is the result observed from the figure, which is shown in the next section using specific statistical tools and mathematical modeling.

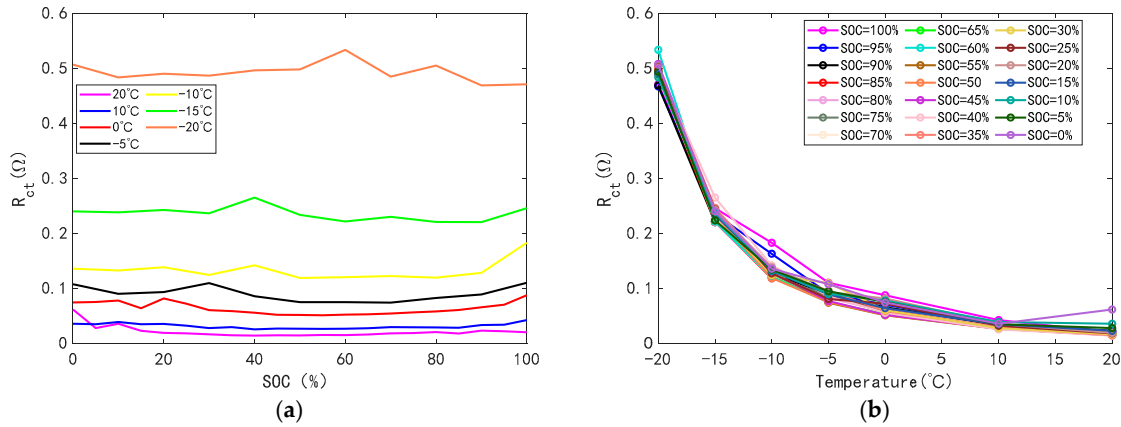


Figure 7. Dependence on measurement conditions of charge transfer resistance R_{ct} : (a) R_{ct} versus SOC curve; (b) R_{ct} versus temperature curve.

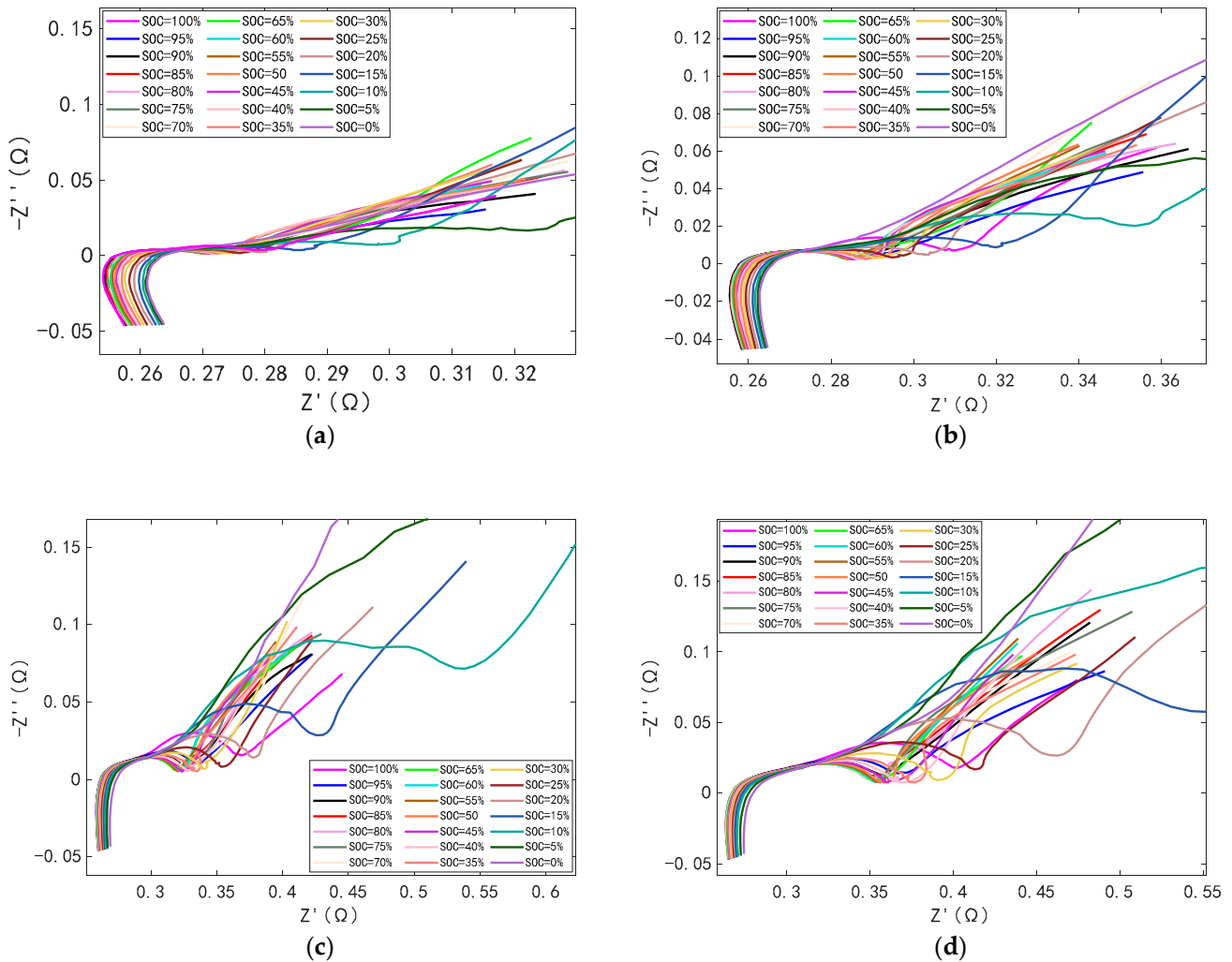


Figure 8. Cont.

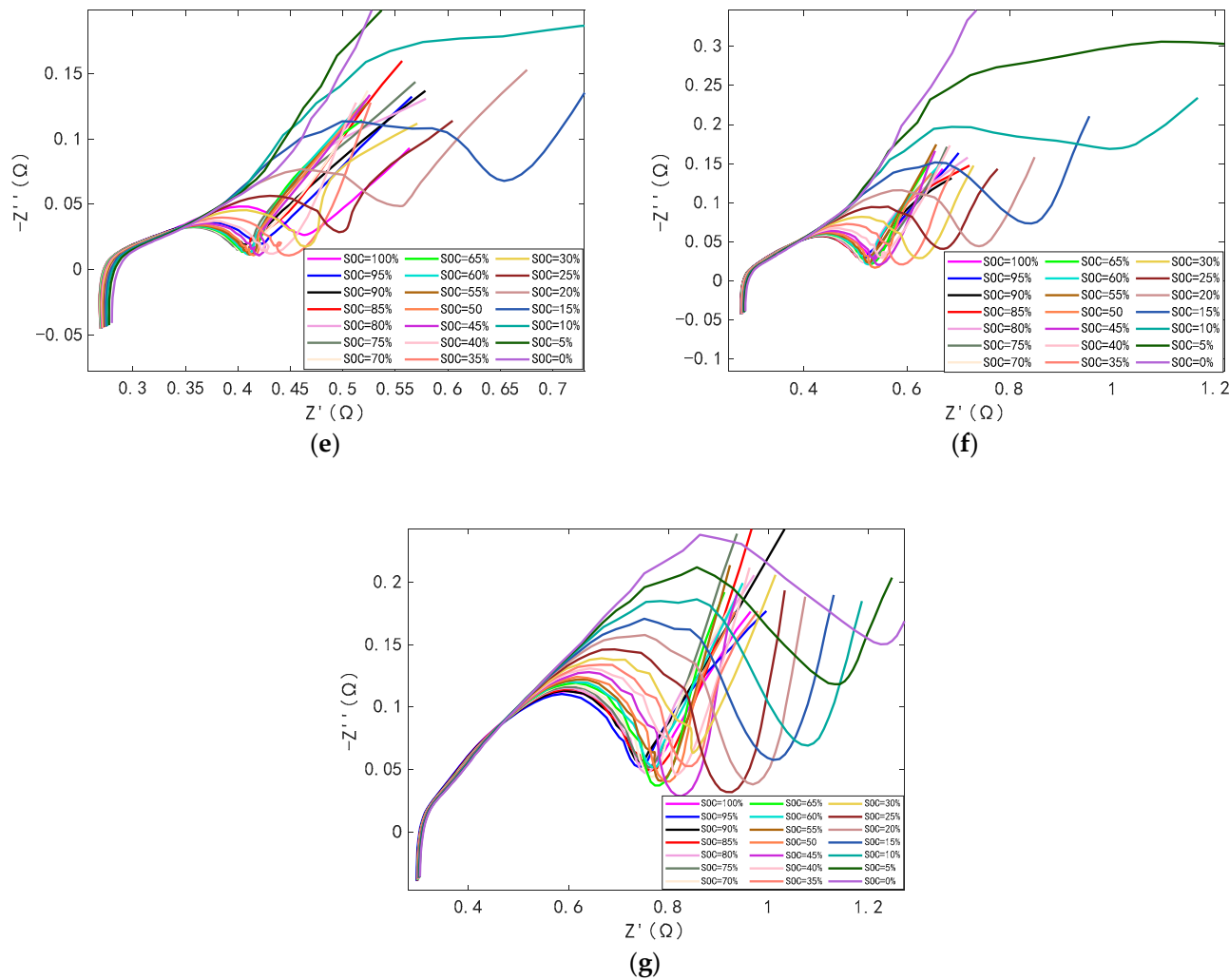


Figure 8. Electrochemical impedance spectra at different temperatures: (a) $T = 20\text{ }^{\circ}\text{C}$; (b) $T = 10\text{ }^{\circ}\text{C}$; (c) $T = 0\text{ }^{\circ}\text{C}$; (d) $T = -5\text{ }^{\circ}\text{C}$; (e) $T = -10\text{ }^{\circ}\text{C}$; (f) $T = -15\text{ }^{\circ}\text{C}$; (g) $T = -20\text{ }^{\circ}\text{C}$.

4. Discussion

To accurately depict the link between the characteristic impedance of Li-ion ternary batteries and the temperature and the SOC of the battery, we need to not only analyze the trend of their interactions qualitatively but also to perform an in-depth quantitative analysis and construct a mathematical model. In the field of statistics, a regression analysis can reveal correlations between variables by analyzing a large number of observations and help to understand the main quantitative relationships between these variables. With this approach, we can more accurately predict and understand how the characteristic impedance varies with temperature and SOC.

4.1. Regression Analysis of Resistance and Temperature

The relationship between the characteristic impedance of the cell (including R_0 , R_{SEI} , and R_{ct}) and the temperature is nonlinear, and this relationship can be described by the Arrhenius equation [39,40]. The equation for the variation in characteristic impedance with temperature can be expressed as follows:

$$1/R_x(T) = A \cdot \exp(-E_a/R/T) \quad (7)$$

where $R_x(T)$ is the battery characteristic impedance including R_0 , R_{SEI} , and R_{ct} ; E_a is the activation energy; $T[K]$ is the temperature; $A[\Omega^{-1}]$ is a constant of proportionality; and R is the gas constant. For ease of handling, this equation can be converted to a linear form:

$$\ln(R_x(T)) = -\ln(A) + E_a/R/T \quad (8)$$

By applying the least squares method to the regression coefficients of the linear model, a linear regression equation for the characteristic impedance and temperature can be obtained. The fitted curves are shown in Figure 9. The obtained fitting coefficients R^2 are all greater than 0.9. R_0 is less affected by temperature, while R_{SEI} and R_{ct} are more affected by temperature.

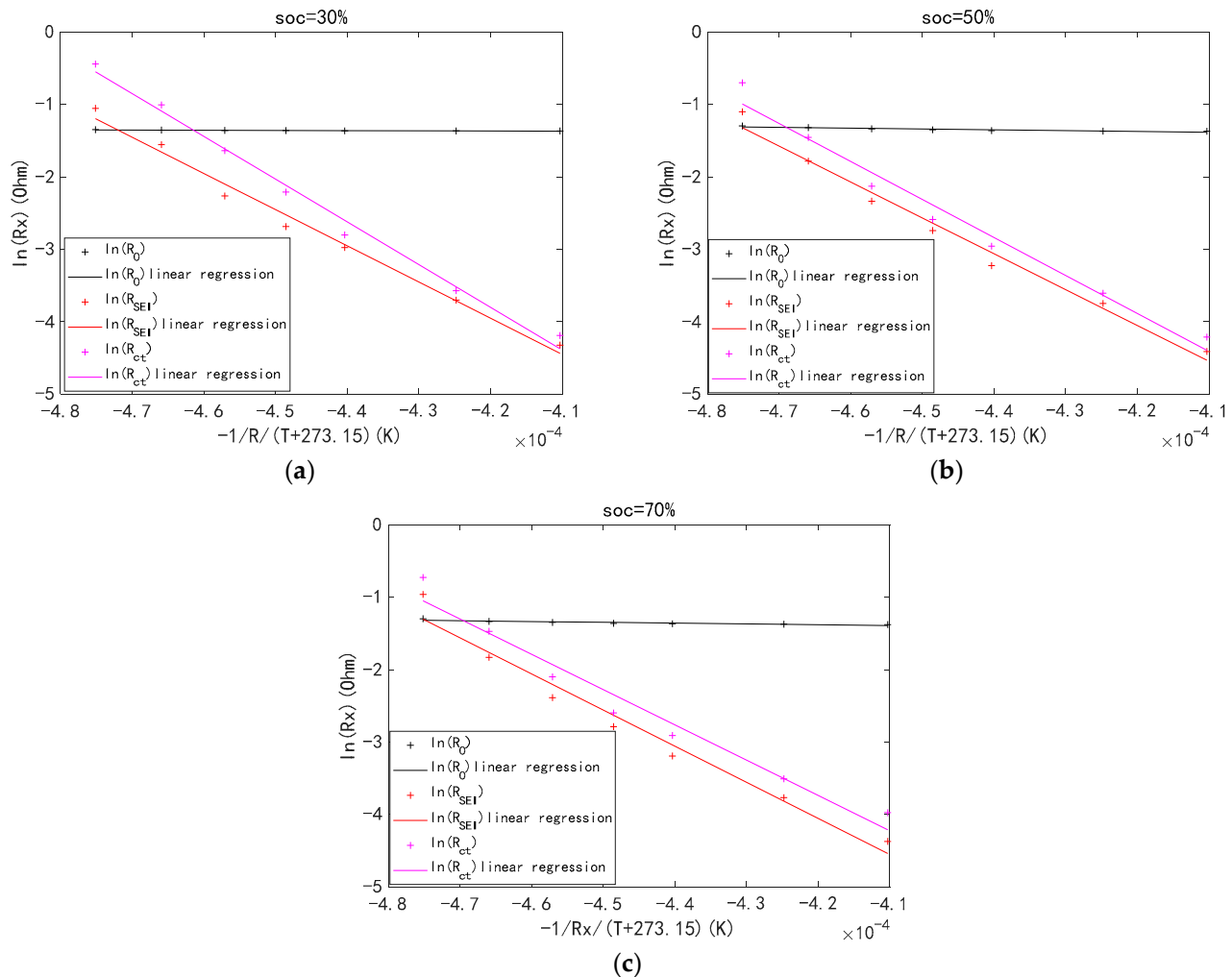


Figure 9. Temperature regression curves of characteristic impedance: (a) Arrhenius linear regression curve for R_x at 30% SOC; (b) Arrhenius linear regression curve for R_x at 50% SOC; (c) Arrhenius linear regression curve for R_x at 70% SOC.

4.2. Regression Analysis of Resistance and SOC

In Figure 10, the three resistor values, R_0 , R_{SEI} , and R_{ct} , show a certain regularity with SOC, manifested as periodic peaks and valleys. This trend can be modeled by a polynomial function, described as the following regression equation:

$$R_X(SOC) = \sum_{i=0}^N \alpha_i SOC^i \quad (9)$$

where α_i is the polynomial coefficient; N is the order of the function. We compare the equations from the first to the sixth order. Although the sixth-order polynomial model fits best, overfitting occurs given the complexity of the model. The third-order polynomials were not overfitted and were well fitted with R^2 greater than 0.9 in all cases.

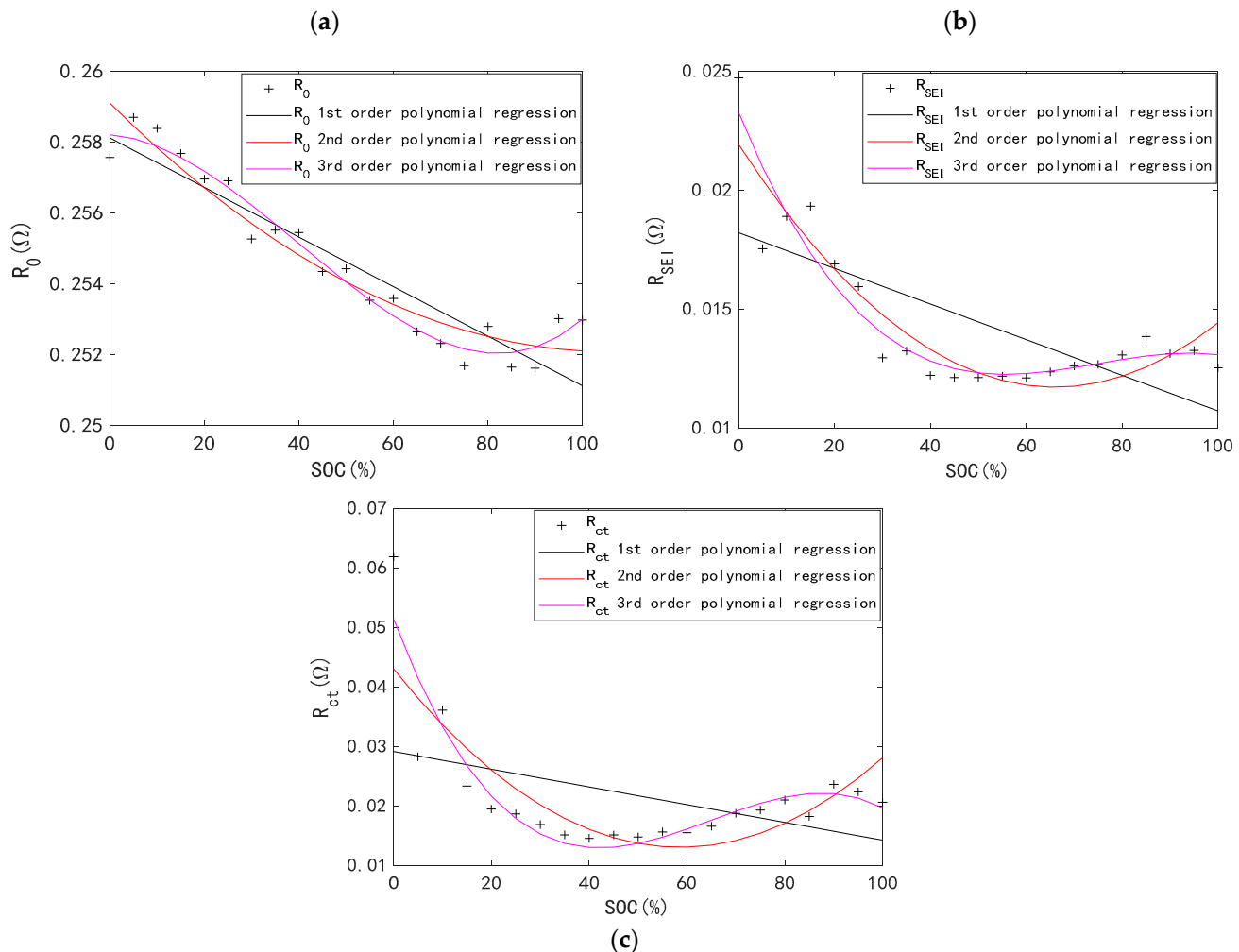


Figure 10. Temperature regression curves for characteristic impedance: (a) R_0 ; (b) R_{SEI} ; and (c) R_{ct} .

4.3. ANOVA Tables for R_0 , R_{SEI} , and R_{ct}

The source of variance (Source) in the ANOVA table indicates the different factors considered in the analysis, i.e., temperature and SOC. The sum of squares of deviations (SS) indicates the sum of squares of the differences between the data at each level and the overall mean. Degrees of freedom (df) indicates the number of parameters that can be varied freely. Mean square (MS) indicates the average variation on each degree of freedom, calculated as the sum of squared deviations divided by the degrees of freedom. F is the mean square ratio, used to test the significance of variation from different sources. The p -value indicates the probability that the observed data or more extreme data will be significant in the hypothesis test.

From a statistical point of view, a p -value of less than 0.05 indicates a significant difference, while a p -value of more than 0.05 indicates a non-significant difference. As shown in Tables 3–5, R_0 varies insignificantly with both temperature and SOC, R_{SEI} is more affected by temperature, and R_{ct} varies significantly with both temperature and SOC, but is more affected by temperature. This result validates the qualitative analysis presented in Section 3 regarding the effect of SOC and temperature on the battery impedance.

Table 3. R_0 ANOVA table.

Source	SS	df	MS	F	p-Value
T	0.00140	6	0.00023	1.09657	0.36843
SOC	0.00422	20	0.00021	0.98801	0.48144
Errors	0.02559	120	0.00021		
Total	0.03121	146			

Table 4. R_{SEI} ANOVA table.

Source	SS	df	MS	F	p-Value
T	2.87871	6	0.47978	94.39260	4.69503×10^{-43}
SOC	0.17989	20	0.00899	1.76963	0.03160
Errors	0.60994	120	0.00508		
Total	3.66855	146			

Table 5. R_{ct} ANOVA table.

Source	SS	df	MS	F	p-Value
T	9.17838	6	1.529731	8.636748	8.21953×10^{-8}
SOC	9.14384	20	0.457192	2.581271	0.000802
Errors	21.25426	120	0.177119		
Total	39.57648	146			

4.4. Impedance Versus Frequency

Figures 11 and 12 show the impedance vs. frequency curves for the battery. According to the impedance model in Section 2, the impedance curves are divided into four frequency ranges as shown in Figure 11a. Battery impedance increases more and more as the temperature decreases, as shown in Figure 12. In addition, as the frequency increases, the impedance tends to become smaller and then increase. When the frequency rises from 0.001 Hz to 0.01 Hz, the impedance decreases sharply; this phase corresponds to the diffusion process within the cell as characterized by Warburg diffusion. When the frequency rises from 0.01 Hz to 20 Hz, the impedance begins to decrease slowly; this phase corresponds to the charge transfer process in the electrode reaction. When the frequency rises from 20 Hz to 3.1 kHz, the impedance decreases with frequency at an almost constant slope; this phase corresponds to the diffusion of Li⁺ through the insulating layer on the surface of the electrode active material. When the frequency rises from 3.1 kHz to 10 kHz, the impedance tends to increase slightly with frequency. This phase corresponds to the inductive impedance generated by electrons passing through the wire and the internal electrode winding, and the process of ions and electrons passing from the electrode interface to the solution and through the pores of the activated carbon.

According to Figure 11b–d, the battery impedance increases significantly as the SOC decreases. When the frequency is between 0.01 Hz and 20 Hz, the impedance increases when the SOC decreases from 0% to 50%; however, the impedance evolution when the SOC changes from 55% to 100% is not obvious. When the frequency exceeds 20 Hz, the battery impedance increases as SOC decreases in the entire SOC range. The impedance increases continuously with SOC when the frequency goes from 20 Hz to 3.1 kHz. As the frequency goes from 3.1 kHz to 10 kHz, the impedance decreases with the increase in SOC.

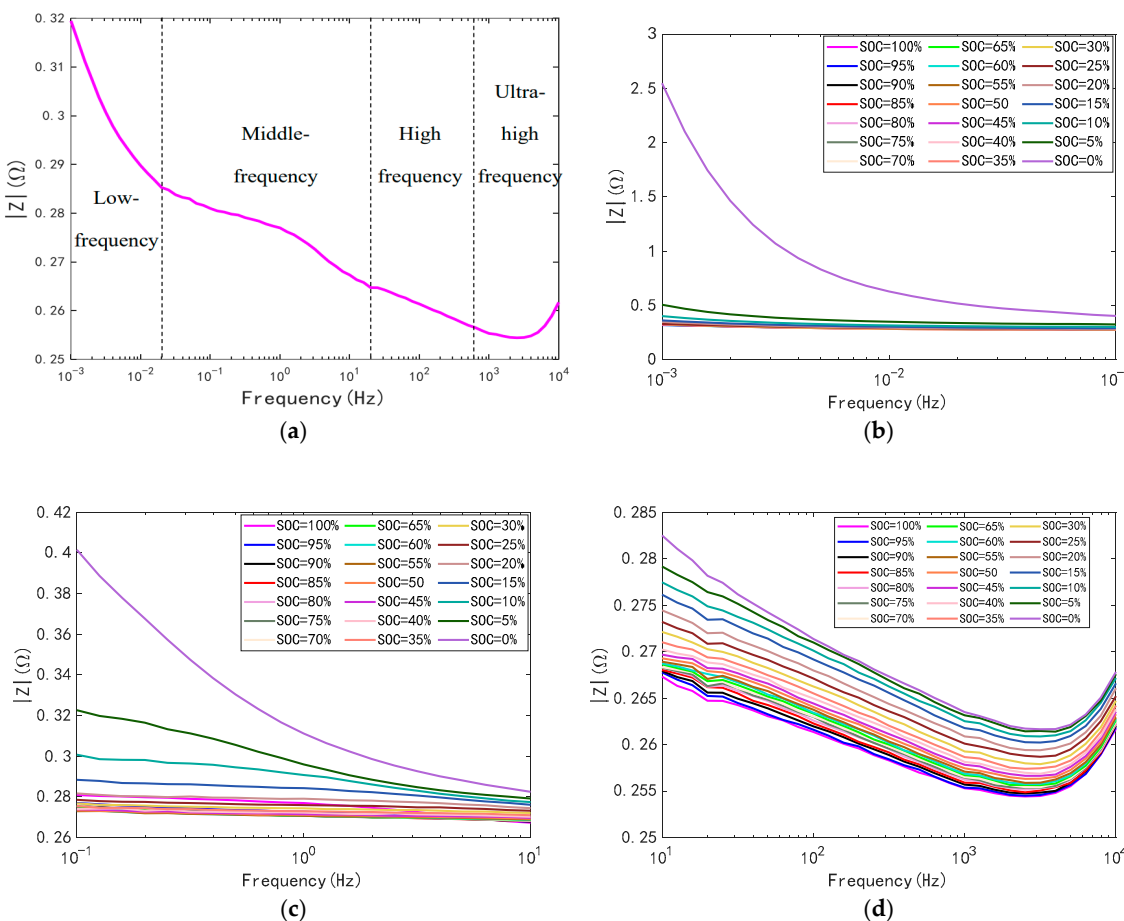


Figure 11. Bode plots at 20 °C: (a) SOC = 100%; (b) frequency = 10^{-3} – 10^{-1} Hz; (c) frequency = 10^{-1} – 10^1 Hz; (d) frequency = 10^1 – 10^4 Hz.

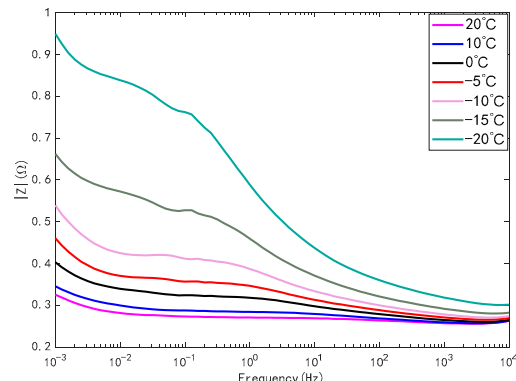


Figure 12. Curve of impedance versus frequency of battery at different temperatures for SOC = 50%.

The point between the two semicircles of the impedance spectrum corresponds to a frequency of 20 Hz at different temperatures and SOCs. The frequencies corresponding to the intersection of the impedance spectrum with the real axis and the point where the impedance spectrum starts to spread vary at different temperatures and SOCs. Therefore, 20 Hz is selected as a specific frequency point to establish the temperature–SOC–impedance model. The impedance spectrum with a temperature of -20 °C and SOC of 50% is selected to extract the other two frequency points. That is, the frequency 3100 Hz corresponds to the intersection point with the real axis and the frequency 1 Hz corresponds to the point where the impedance spectrum starts to spread. The impedance variation with temperature and SOC at 20 Hz has a similar pattern to R_0 , R_{SEI} , and R_{ct} ; i.e., there is an approximately

exponential dependence of impedance on temperature, as shown in Figure 13a. Impedance and SOC follows a polynomial function model, as shown in Figure 13b. Impedance dependence on SOC then follows a polynomial function model, as shown in Figure 11a,b. Considering the effect of two factors on impedance, the temperature–SOC-based impedance model is established, as shown in Equation (10). To facilitate the calculation, the model is simplified as shown in Equation (11).

$$1/|Z|(T, SOC) = |Z|_A(SOC) \cdot \exp(-|Z|_{E_a}(SOC)/R/T) \quad (10)$$

$$\ln(|Z|(T, SOC)) = -\ln(|Z|_A(SOC)) + |Z|_{E_a}(SOC)/R/T \quad (11)$$

$$|Z|_A(SOC) = \sum_{i=0}^N \alpha_{i,A} SOC^i \quad (12)$$

$$|Z|_{E_a}(SOC) = \sum_{i=0}^N \alpha_{i,E_a} SOC^i \quad (13)$$

where $1/|Z|(T, SOC)$ denotes a function of the parameters of the model at different temperatures and SOCs, $|Z|_A(SOC)$ denotes a polynomial function of the proportionality constant A, and $|Z|_{E_a}(SOC)$ denotes functions of the activation energy E_a . $\alpha_{i,A}$ and α_{i,E_a} are the polynomial coefficients of the i -th order of the proportionality constant polynomial and the activation energy polynomial function, respectively.

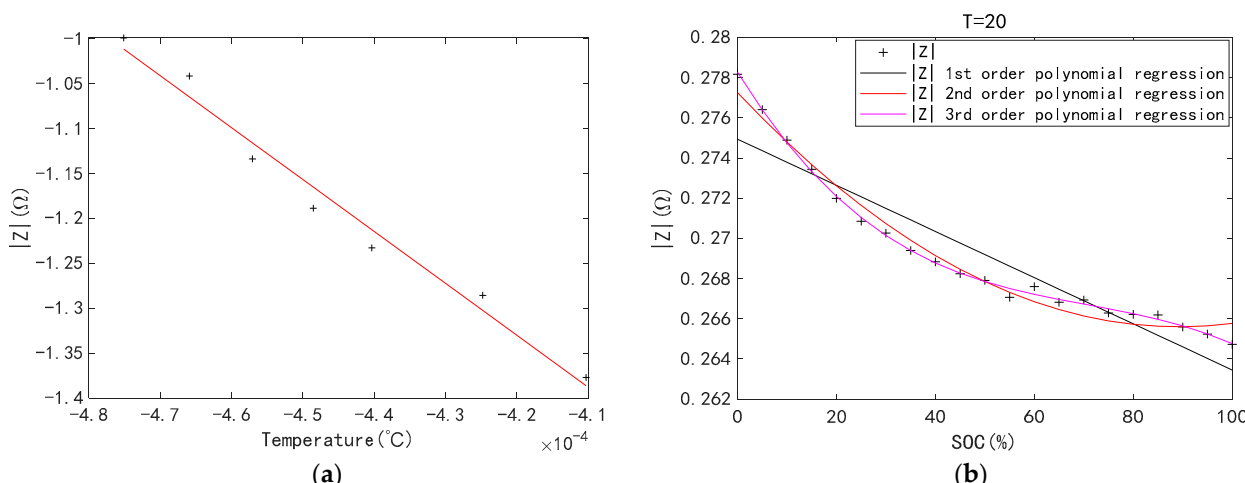


Figure 13. Impedance versus temperature and SOC: (a) linear regression curve of impedance versus temperature; (b) polynomial regression curves of SOC versus impedance.

As shown in Figures 14 and 15 and Table 6, the fitting accuracies, model parameters, and model precision are compared for the three frequencies. For SOC between 40% and 60% and temperatures between 0°C and 20°C , the best fit is obtained at a frequency of 20 Hz. At this time, R^2 is 0.98 and the root mean square error (RMSE) is 0.007. For SOCs between 20% and 80% and temperatures between -20°C and 20°C , the model developed for the frequency of 1 Hz cannot estimate the impedance dependence on SOC and temperature. For the same conditions, the model developed for 20 Hz estimates better than the model developed for 3100 Hz (0.85 vs. 0.75 R^2 , 0.055 vs. 0.060 RMSE), involving the dependence on SOC and temperature. Therefore, the model developed for a frequency of 20 Hz has the best impedance estimation accuracy for a wide range of temperatures and SOCs.

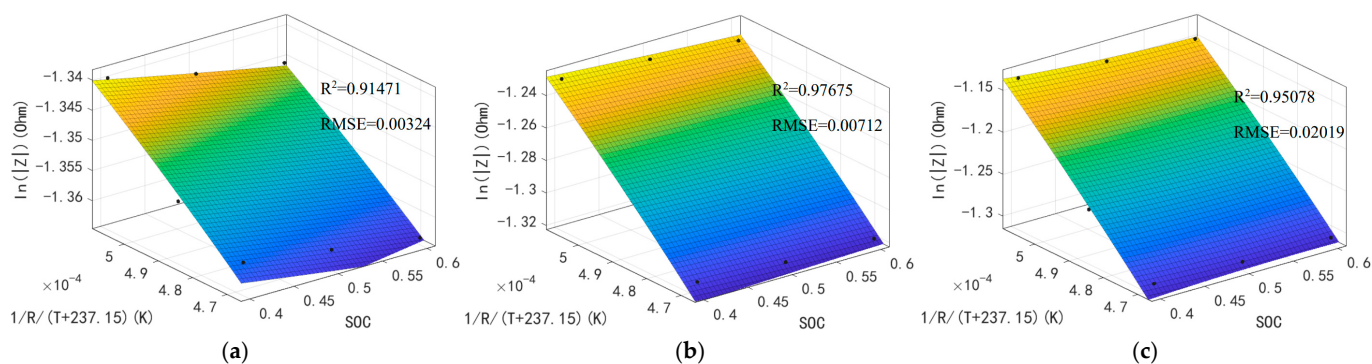


Figure 14. Fitted results for SOC of 40% to 60% and temperatures of 0 °C to 20 °C: (a) the frequency is 3100 Hz; (b) the frequency is 20 Hz; (c) the frequency is 1 Hz.

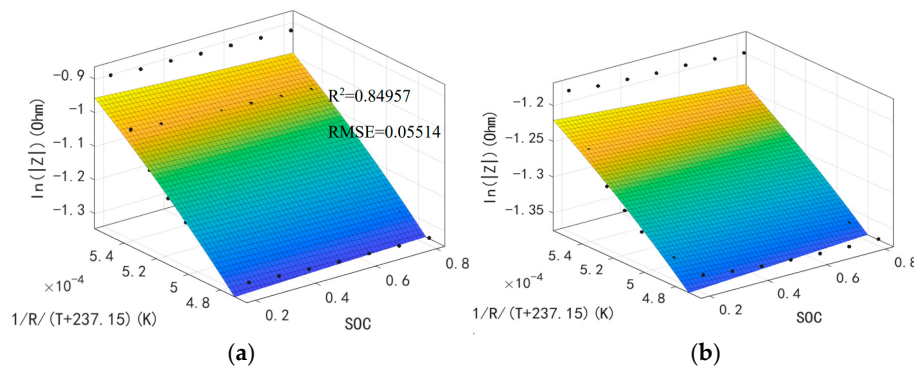


Figure 15. Fitted results for SOC of 20% to 80% and temperatures of −20 °C to 20 °C: (a) the frequency is 3100 Hz; (b) the frequency is 20 Hz.

Table 6. Temperature–SOC-Impedance Modeling Factor table.

Ranges	Temperature Range (°C)	SOC Range (%)	Frequency (Hz)	$\alpha_{0,A}$	$\alpha_{1,A}$	α_{0,E_a}	α_{1,E_a}	R^2	RMSE
Narrow	[0, 20]	[40, 60]	3100	2.8700	0.4097	−0.0001	0.0001	0.91471	0.00324
			20	1.1437	0.2781	−0.0005	0.0001	0.97675	0.00712
			1	0.3186	0.2959	−0.0011	0.0003	0.95078	0.02019
Wide	[−20, 20]	[20, 80]	3100	1.4471	0.1018	−0.0005	0.0000	0.75294	0.06018
			20	0.3086	0.0535	−0.0012	0.0001	0.84957	0.05514
			1	\	\	\	\	\	\

5. Conclusions

This paper investigates the effect of different frequencies on the accuracy of the battery impedance estimation model. EIS measurements are performed on NCR18650 cells at seven temperatures and 21 SOCs. An Arrhenius model of R_0 , R_{SEI} , and R_{ct} versus temperature and a polynomial regression model versus SOC were developed. It was observed that temperature has a greater effect on R_0 , R_{SEI} , and R_{ct} than the SOC. Then, a binary ANOVA table was created to numerically conclude that R_0 , R_{SEI} , and R_{ct} are more significantly affected by temperature. Finally, the temperature–SOC-impedance model is developed at three specific frequency points, i.e., 3100 Hz, 20 Hz, and 1 Hz. In narrow temperature and SOC ranges, the developed impedance estimation models for the three frequency points show a good performance, with the highest at 20 Hz. In the wide temperature and SOC ranges, the model cannot be used to characterize the relationship between SOC, temperature, and impedance at 1 Hz, while the impedance estimation accuracy at 20 Hz is higher than that at 3100 Hz. This work’s key finding is that the impedance model accuracy is highest at 20 Hz. This provides reference frequency points for accurate online impedance measurement in the wide

temperature and wide SOC range, laying the foundation for obtaining more accurate battery state estimation based on impedance models in battery management systems.

Author Contributions: Conceptualization, J.M. and X.H.; methodology, J.M.; software, Y.Z.; validation, J.M. and D.-I.S.; formal analysis, Y.X. and X.H.; investigation, J.M. and D.-I.S.; resources, Y.X. and X.H.; data curation, Y.X. and X.H.; writing—original draft preparation, Y.X. and X.H.; writing—review and editing, J.M., V.K. and D.-I.S.; visualization, D.-I.S.; supervision, Y.Z.; project administration, Y.Z.; funding acquisition, X.H. and Y.Z. All authors have read and agreed to the published version of the manuscript.

Funding: This research was funded by the National Key R&D plan Foundation of China (2021YFB1600200); the National Natural Science Foundation of China (52407236); the Qinchuangyuan High-Level Innovation and Entrepreneurship Talent Program of Shaanxi (QCYRCXM-2023-112); the Fundamental Research Funds for the Central Universities, CHD (300102383202); and the Natural Science Basic Research Program of Shaanxi (2023-JC-QN-0437).

Data Availability Statement: The original contributions presented in the study are included in the article, further inquiries can be directed to the corresponding author.

Conflicts of Interest: The authors declare no conflicts of interest.

References

- IEA. Trends in electric cars. In *Global EV Outlook 2024*; IEA: Paris, France, 2024.
- Arsalis, A.; Papanastasiou, P.; Georghiou, G.E. A comparative review of lithium-ion battery and regenerative hydrogen fuel cell technologies for integration with photovoltaic applications. *Renew. Energy* **2022**, *191*, 943–960. [[CrossRef](#)]
- Peng, F.; Xie, X.; Wu, K.; Zhao, Y.; Ren, L. Online hierarchical energy management strategy for fuel cell based heavy-duty hybrid power systems aiming at collaborative performance enhancement. *Energy Convers. Manag.* **2023**, *276*, 116501. [[CrossRef](#)]
- Carthy, K.M.; Gullapalli, H.; Ryan, K.M.; Kennedy, T. Review-Use of Impedance Spectroscopy for the Estimation of Li-ion Battery State of Charge, State of Health and Internal Temperature. *J. Electrochem. Soc.* **2021**, *168*, 080517. [[CrossRef](#)]
- Zou, Y.; Hu, X.; Ma, H.; Li, S.E. Combined State of Charge and State of Health estimation over lithium-ion battery cell cycle lifespan for electric vehicles. *J. Power Sources* **2015**, *273*, 793–803. [[CrossRef](#)]
- Saha, B.; Goebel, K.; Poll, S.; Christoffersen, J. Prognostics Methods for Battery Health Monitoring Using a Bayesian Framework. *IEEE Trans. Instrum. Meas.* **2009**, *58*, 291–296. [[CrossRef](#)]
- McCarthy, K.; Gullapalli, H.; Ryan, K.M.; Kennedy, T. Electrochemical impedance correlation analysis for the estimation of Li-ion battery state of charge, state of health and internal temperature. *J. Energy Storage* **2022**, *50*, 104608. [[CrossRef](#)]
- Zhang, G.; Wei, X.; Han, G.; Dai, H.; Zhu, J.; Wang, X.; Tang, X.; Ye, J. Lithium plating on the anode for lithium-ion batteries during long-term low temperature cycling. *J. Power Sources* **2021**, *484*, 229312. [[CrossRef](#)]
- Zhu, J.; Darma, M.S.D.; Knapp, M.; Sorensen, D.R.; Heere, M.; Fang, Q.; Wang, X.; Dai, H.; Mereacre, L.; Senyshyn, A.; et al. Investigation of lithium-ion battery degradation mechanisms by combining differential voltage analysis and alternating current impedance. *J. Power Sources* **2020**, *448*, 227575. [[CrossRef](#)]
- Zhu, J.; Knapp, M.; Liu, X.; Yan, P.; Dai, H.; Wei, X.; Ehrenberg, H. Low-Temperature Separating Lithium-Ion Battery Interfacial Polarization Based on Distribution of Relaxation Times (DRT) of Impedance. *Ieee Trans. Transp. Electrif.* **2021**, *7*, 410–421. [[CrossRef](#)]
- Kassem, M.; Delacourt, C. Postmortem analysis of calendar-aged graphite/LiFePO₄ cells. *J. Power Sources* **2013**, *235*, 159–171. [[CrossRef](#)]
- Westerhoff, U.; Kurbach, K.; Lienesch, F.; Kurrat, M. Analysis of Lithium-Ion Battery Models Based on Electrochemical Impedance Spectroscopy. *Energy Technol.* **2016**, *4*, 1620–1630. [[CrossRef](#)]
- Seaman, A.; Dao, T.-S.; McPhee, J. A survey of mathematics-based equivalent-circuit and electrochemical battery models for hybrid and electric vehicle simulation. *J. Power Sources* **2014**, *256*, 410–423. [[CrossRef](#)]
- Doyle, M.; Fuller, T.F.; Newman, J. Modeling of galvanostatic charge and discharge of the lithium/polymer/insertion cell. *J. Electrochem. Soc.* **1993**, *140*, 1526–1533. [[CrossRef](#)]
- Bizeray, A.M.; Zhao, S.; Duncan, S.R.; Howey, D.A. Lithium-ion battery thermal-electrochemical model-based state estimation using orthogonal collocation and a modified extended Kalman filter. *J. Power Sources* **2015**, *296*, 400–412. [[CrossRef](#)]
- Zhang, H.; Deng, C.; Zong, Y.; Zuo, Q.; Guo, H.; Song, S.; Jiang, L. Effect of Sample Interval on the Parameter Identification Results of RC Equivalent Circuit Models of Li-ion Battery: An Investigation Based on HPPC Test Data. *Batteries* **2023**, *9*, 1. [[CrossRef](#)]

17. Pastor-Fernandez, C.; Uddin, K.; Chouchelamane, G.H.; Widanage, W.D.; Marco, J. A Comparison between Electrochemical Impedance Spectroscopy and Incremental Capacity-Differential Voltage as Li-ion Diagnostic Techniques to Identify and Quantify the Effects of Degradation Modes within Battery Management Systems. *J. Power Sources* **2017**, *360*, 301–318. [[CrossRef](#)]
18. Choi, W.; Shin, H.-C.; Kim, J.M.; Choi, J.-Y.; Yoon, W.-S. Modeling and Applications of Electrochemical Impedance Spectroscopy (EIS) for Lithium-ion Batteries. *J. Electrochem. Sci. Technol.* **2020**, *11*, 1–13. [[CrossRef](#)]
19. Meng, J.; Du, X.; Peng, J.; Lin, M.; Song, Z. Rapid Lithium-Ion Battery Impedance Measurements Using Binary Sequence With Optimized Frequency Components. *IEEE Trans. Ind. Electron.* **2024**, *71*, 7190–7198. [[CrossRef](#)]
20. Meng, J.; Peng, J.; Cai, L.; Song, Z. Rapid Impedance Extraction for Lithium-Ion Battery by Integrating Power Spectrum and Frequency Property. *IEEE Trans. Ind. Electron.* **2024**, *71*, 7220–7229. [[CrossRef](#)]
21. Wang, L.; Zhao, X.; Deng, Z.; Yang, L. Application of electrochemical impedance spectroscopy in battery management system: State of charge estimation for aging batteries. *J. Energy Storage* **2023**, *57*, 106275. [[CrossRef](#)]
22. Wang, Q.-K.; He, Y.-J.; Shen, J.-N.; Hu, X.-S.; Ma, Z.-F. State of Charge-Dependent Polynomial Equivalent Circuit Modeling for Electrochemical Impedance Spectroscopy of Lithium-Ion Batteries. *IEEE Trans. Power Electron.* **2018**, *33*, 8449–8460. [[CrossRef](#)]
23. Kong, L.; Fang, S.; Niu, T.; Chen, G.; Yang, L.; Liao, R. Fast State of Charge Estimation for Lithium-ion Battery Based on Electrochemical Impedance Spectroscopy Frequency Feature Extraction. *IEEE Trans. Ind. Appl.* **2024**, *60*, 1369–1379. [[CrossRef](#)]
24. Zhang, Q.; Huang, C.-G.; Li, H.; Feng, G.; Peng, W. Electrochemical Impedance Spectroscopy Based State-of-Health Estimation for Lithium-Ion Battery Considering Temperature and State-of-Charge Effect. *IEEE Trans. Transp. Electrif.* **2022**, *8*, 4633–4645. [[CrossRef](#)]
25. Jiang, B.; Zhu, J.; Wang, X.; Wei, X.; Shang, W.; Dai, H. A comparative study of different features extracted from electrochemical impedance spectroscopy in state of health estimation for lithium-ion batteries. *Appl. Energy* **2022**, *322*, 119502. [[CrossRef](#)]
26. Zhu, J.G.; Sun, Z.C.; Wei, X.Z.; Dai, H.F. A new lithium-ion battery internal temperature on-line estimate method based on electrochemical impedance spectroscopy measurement. *J. Power Sources* **2015**, *274*, 990–1004. [[CrossRef](#)]
27. Beelen, H.P.G.J.; Raijmakers, L.H.J.; Donkers, M.C.F.; Notten, P.H.L.; Bergveld, H.J. An improved impedance-based temperature estimation method for Li-ion batteries. *IFAC-Pap. Online* **2015**, *48*, 383–388. [[CrossRef](#)]
28. Mc Carthy, K.; Gullapalli, H.; Kennedy, T. Real-time internal temperature estimation of commercial Li-ion batteries using online impedance measurements. *J. Power Sources* **2022**, *519*, 230786. [[CrossRef](#)]
29. Li, R.; Wu, J.; Wang, H.; Li, G. Prediction of state of charge of Lithium-ion rechargeable battery with electrochemical impedance spectroscopy theory. In Proceedings of the 2010 5th IEEE Conference on Industrial Electronics and Applications, Taichung, Taiwan, 15–17 June 2010; pp. 684–688.
30. Schmidt, J.P.; Arnold, S.; Loges, A.; Werner, D.; Wetzel, T.; Ivers-Tiffée, E. Measurement of the internal cell temperature via impedance: Evaluation and application of a new method. *J. Power Sources* **2013**, *243*, 110–117. [[CrossRef](#)]
31. Beelen, H.P.G.J.; Raijmakers, L.H.J.; Donkers, M.C.F.; Notten, P.H.L.; Bergveld, H.J. A comparison and accuracy analysis of impedance-based temperature estimation methods for Li-ion batteries. *Appl. Energy* **2016**, *175*, 128–140. [[CrossRef](#)]
32. Spinner, N.S.; Love, C.T.; Rose-Pehrsson, S.L.; Tuttle, S.G. Expanding the Operational Limits of the Single-Point Impedance Diagnostic for Internal Temperature Monitoring of Lithium-ion Batteries. *Electrochim. Acta* **2015**, *174*, 488–493. [[CrossRef](#)]
33. Richardson, R.R.; Ireland, P.T.; Howey, D.A. Battery internal temperature estimation by combined impedance and surface temperature measurement. *J. Power Sources* **2014**, *265*, 254–261. [[CrossRef](#)]
34. Srinivasan, R. Monitoring dynamic thermal behavior of the carbon anode in a lithium-ion cell using a four-probe technique. *J. Power Sources* **2012**, *198*, 351–358. [[CrossRef](#)]
35. Waag, W.; Fleischer, C.; Sauer, D.U. Critical review of the methods for monitoring of lithium-ion batteries in electric and hybrid vehicles. *J. Power Sources* **2014**, *258*, 321–339. [[CrossRef](#)]
36. Zhuang, Q.; Yang, Z.; Zhang, L.; Cui, Y. Research Progress on Diagnosis of Electrochemical Impedance Spectroscopy in Lithium Ion Batteries. *Prog. Chem.* **2020**, *32*, 761–791. [[CrossRef](#)]
37. Yamashiro, S.; Nakamura, K. Equivalent Circuit Model for Electric Double Layer Capacitors and its Applications. *Electr. Eng. Jpn.* **2012**, *180*, 29–37. [[CrossRef](#)]
38. von Srbik, M.-T.; Marinescu, M.; Martinez-Botas, R.F.; Offer, G.J. A physically meaningful equivalent circuit network model of a lithium-ion battery accounting for local electrochemical and thermal behaviour, variable double layer capacitance and degradation. *J. Power Sources* **2016**, *325*, 171–184. [[CrossRef](#)]
39. Waag, W.; Kaebitz, S.; Sauer, D.U. Experimental investigation of the lithium-ion battery impedance characteristic at various conditions and aging states and its influence on the application. *Appl. Energy* **2013**, *102*, 885–897. [[CrossRef](#)]
40. Feng, F.; Yang, R.; Meng, J.; Xie, Y.; Zhang, Z.; Chai, Y.; Mou, L. Electrochemical impedance characteristics at various conditions for commercial solid-liquid electrolyte lithium-ion batteries: Part. 2. Modeling and prediction. *Energy* **2022**, *243*, 123091. [[CrossRef](#)]